Metallic Elements inside a Mismatched Luneburg Lens: Experimental Validation at V-band

Vincent Kaschten*†, Dimitri Lederer*, Christophe Craeye*,
*ICTEAM Institute, UCLouvain, Louvain-la-Neuve, Belgium,
vincent.kaschten@uclouvain.be, dimitri.lederer@uclouvain.be, christophe.craeye@uclouvain.be
†BEA Sensors Europe, Liège, Belgium

***Abstract*—We implement a cylindrical mismatched Luneburg lens on PCB at V-band, including metallic elements inside the GRIN lens. The lens has a relative dielectric permittivity of 2.2 at its edge, while the exterior medium is air. The judicious choice of dielectric substrate, and the introduction of metallic posts at carefully selected positions, both enhance the bandwidth and radiation properties of the GRIN lens antenna. Measurements confirm that this design can produce a stable fan-shaped beam over a 10 GHz bandwidth and at multiple excitation points covering a 90 degree angular range.**

***Index Terms*—GRIN lenses, Luneburg lens, mismatched Luneburg lens, PCB, GCPW, SIW, Whispering Gallery Modes, bandwidth enhancement, radiation properties enhancement.**

I. Introduction

The Luneburg lens [1] is a type of Gradient-Index (GRIN) lens, i.e. a non-homogeneous yet spherically/cylindrically symmetric lens whose refractive index variation leads to the collimation of the radiation coming from a point source. Despite its attractive properties, such as the ability to switch beams with low scan loss and high gain [2], the difficulty of realization of such a lens has limited its use at high frequencies [3]. For a wide range of technologies [4], the main difficulty lies in realizing the complete refractive index profile. It has recently been proposed, in order to ease the fabrication process, to improve the design flexibility lying in the choice of lens profile to be implemented: either by decreasing the maximum value [5] or increasing the minimum value [3][4] of refractive index inside the lens.

The second option combines the principles of a virtual image lens and an extended hemispherical lens [3]; in other words it combines a GRIN effect and an interface effect [4]. That results in a lens that is no longer matched with the exterior medium: this causes internal reflections, circulating along the perimeter of the lens, and generating Whispering Gallery Modes that lead to drops of radiation efficiency [6] at specific frequencies. Techniques to mitigate the effect of such WGMs have been proposed in [4], including the introduction of metallic posts inside the GRIN lens, which has already been used to enhance radiation properties in a Gutman lens [7].

In this paper, we implement a cylindrical *Mismatched Luneburg Lens* [4] following a square law along the (normalized) radial coordinate $r \in [0, 1]$

$$\varepsilon_r(r) = \varepsilon_{center} - (\varepsilon_{center} - \varepsilon_{edge})\ r^2 \qquad (1)$$

between a value ε_{center} at the lens center and ε_{edge} at the lens edge ($r = 1$), linked together by the following relationship:

$$\varepsilon_{center} = 2 + \sqrt{2}\ (\sqrt{\varepsilon_{edge}} - 1) \qquad (2)$$

where the $\sqrt{2}$ coefficient actually is frequency-dependent [8] and corresponds here to a diameter-to-wavelength ratio $D/\lambda_0 = 6$.

This work follows our previous work [2] in which we designed a PCB-integrated GRIN lens antenna, including a GCPW to SIW transition used as a feed. To enlarge the bandwidth of the transition, we now move to a lower dielectric permittivity substrate. Furthermore, to mitigate the WGMs and make the radiation properties of the antenna as stable as possible w.r.t. frequency, we now also introduce metallic elements inside the GRIN lens at carefully selected positions. This work proposes a practical demonstration of the mitigation of WGMs using metallic elements, with additional insightful information about the effects of the latter on the radiation properties, in particular along the third dimension that was not considered by the 2D full-wave solver [4].

This paper is organized as follows. Section II describes the implementation of the *Mismatched Luneburg Lens* on PCB. Section III optimizes the GCPW to SIW transition from our previous work [2] to account for the new dielectric substrate. The transition is used in Section IV as a feed to obtain a GRIN lens antenna. Section V introduces metallic elements inside the GRIN lens to enhance radiation properties. Section VI presents measurement results, while Section VI provides a brief conclusion.

II. Mismatched Luneburg Lens

In this paper, we chose to work with standard substrate and prepreg materials from Rogers, both with a relative dielectric permittivity $\varepsilon_{r,sub} = 3$ (dielectric and metallic losses, including metal roughness, were taken into account in the following simulations). In order to obtain a collimated beamwidth of about 10° we chose a lens radius $R = 15mm$ (i.e., a diameter equal to $6\lambda_0$ at 60 GHz) that we discretized into 15 dielectric zones with a radial expansion of 1mm each, see Fig. 1(a).

Following our previous work [2], we introduced in each zone a certain number of through-holes with a given diameter, drilled over the whole height of the PCB lens (see Fig. 1(c)), leading to an effective permittivity for each zone $\varepsilon_{r,zone}$ according to the effective medium theory [9]. For the

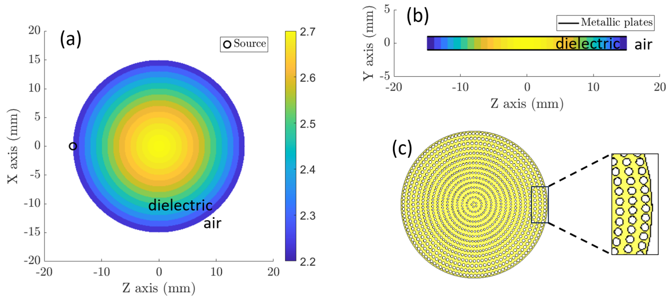

Fig. 1. GRIN lens implementing a mismatched Luneburg distribution discretized into 15 zones (a)-(b) on PCB, by drilling air holes (c).

outermost zone, it was determined that a maximum fraction of air ($\varepsilon_{r,air} = 1$) equal to 40% could be reached (while complying with PCB fabrication constraints), leading to the minimum effective permittivity achievable equal to

$$\min(\varepsilon_{r,zone}) = 40\%\ \varepsilon_{r,air} + 60\%\ \varepsilon_{r,sub} = 2.2 \qquad (3)$$

while that value was equal to 2.6 in our previous work [2], leading to the combination $(\varepsilon_{center}, \varepsilon_{edge}) = (2.9, 2.6)$. In this work, we chose the combination $(\varepsilon_{center}, \varepsilon_{edge}) = (2.7, 2.2)$ according to (2). By appropriate choice of the multi-layer PCB stack-up, the height h_{PCB} from top to bottom layer was fixed at about 2mm (i.e., $0.4\lambda_0$ at 60 GHz) as shown in Fig.1(b), in order to obtain a beamwidth greater than 60° in elevation.

III. GCPW to SIW Transition

The feed structure used to excite the lens is based on our previous work [2] presenting a transition from a 50Ω GCPW to an SIW. The SIW was implemented with vias of diameter $d = 300$ µm spaced by a distance $s = 400$ µm from each other in each row. With the PCB height fixed at $h_{PCB} = h_{SIW} \approx 2$ mm the TE_{01} mode (horizontally polarized, see Fig. 2(b)) has a cutoff frequency $f_c^{TE_{01}} = 43$ GHz. We decided to fix the SIW physical width $a_{SIW,phys}$ at 1.95 mm, which yields a cutoff frequency $f_c^{TE_{10}} = 50$ GHz for the TE_{10} mode (vertically polarized, see Fig. 2(c)) while the higher order modes, e.g. the TE_{11} mode, have a cutoff frequency above $f_c^{TE_{11}} = 66$ GHz.

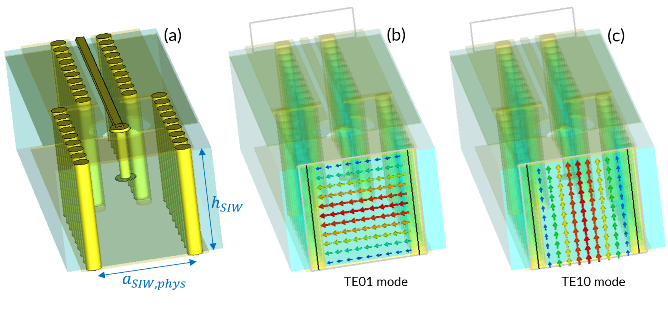

Fig. 2. GCPW to SIW transition, (a) blind via highlighted (along with the signal line of the GCPW and the through vias), (b) TE_{01} (horizontally polarized) and (c) TE_{10} (vertically polarized) modes shown on the SIW side.

The transition was designed following the same coupling mechanism as presented in [2]: a blind via diving into a half-wavelength SIW section, at its center (see Fig. 2(a)). The structure was simulated using CST Studio Suite with port 1 at the GCPW side and port 2 at the SIW side.

The S-parameters of the optimized transition can be found in Fig. 3. Port 1 is matched from 54 GHz to 72 GHz. The various S_{21} parameters, corresponding to the modes that can be excited at port 2, show that the TE_{10} mode is dominant between 54 GHz and 66 GHz with an $S_{21,TE_{10}}$ better than -1.5dB, while the fundamental TE_{01} mode is above cutoff but not excited at all, and higher order modes are still below cutoff. The matching at port 2 in the TE_{10} mode ($S_{22,TE_{10}}$) is achieved from 54 GHz to 66 GHz. To sum up, the transition from GCPW to the TE_{10} mode in the SIW is matched at both ports with an insertion loss around 1.2 dB on a 12 GHz bandwidth, from 54 GHz to 66 GHz.

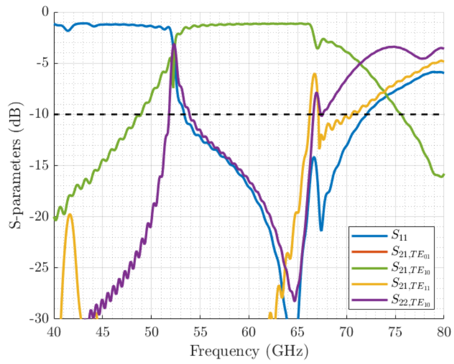

Fig. 3. Simulated S-parameters of the optimized GCPW to SIW transition.

Working with a substrate with lower dielectric permittivity $\varepsilon_{r,sub} = 3$ and losses $\tan\delta \approx 0.0015$ than previously ($\varepsilon_{r,sub} = 3.66$ and $\tan\delta = 0.0037$ in [2]) while maintaining the same PCB height leads to lower insertion losses as well as a bandwidth enhancement of the transition, as highlighted in Table I. This is a result of the desired TE_{10} mode cutoff frequency being 3.5 GHz lower than previously and the undesired higher order modes remaining with cutoff frequencies above 66 GHz. The operational bandwidth of the transition increases from 8 GHz in [2] to 12 GHz here.

TABLE I
Comparison of the optimized design with previous work.

	Previous work [2]	This work
$f_c^{TE_{10}}$ – $f_c^{TE_{11}}$	53.5 GHz – 66 GHz	50 GHz – 66 GHz
Matching at both ports	[56 GHz, 66 GHz]	[54 GHz, 66 GHz]
Insertion loss $S_{21,TE_{10}}$	$<$ 2.5 dB	$<$ 1.5 dB
on frequency band	[57 GHz, 65 GHz]	[54 GHz, 66 GHz]
Plateau value $S_{21,TE_{10}}$	$\approx$ 2 dB	$\approx$ 1.2 dB
Transition bandwidth	8 GHz	12 GHz
Stable fan-shaped beam	[59 GHz, 65 GHz]	[56 GHz, 66 GHz]
GRIN lens bandwidth	6 GHz	10 GHz

IV. GRIN Lens Antenna

The transition detailed in section III is now used as a feed for the GRIN lens detailed in section II. A total of 10 feeds are added, with the SIW end placed tangent to the lens perimeter, see Fig. 4(a). The feeds are placed 10° from each other, and the two outermost ones (numbered 1 and 10) act as dummy ports (as is typically done with Rotman lenses [10]) which stabilize the performance of ports 2 and 9.

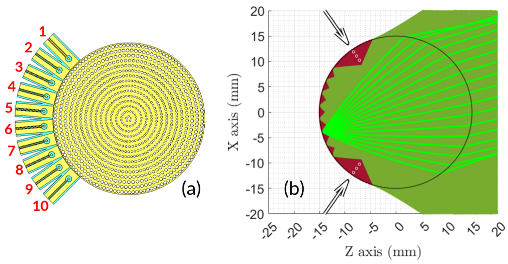

Fig. 4. (a) GRIN lens antenna with 10 feeds on the lens perimeter, with dielectric substrate in blue, copper in yellow, simulations ports (on the GCPW ends, numbered from 1 to 10) in red. (b) Ray paths from port 7, repeated at ports 2-9 to produce the green zone, while the rest of the lens is coloured as the red zone. Metallic elements are represented as white circles.

The optimized S_{ii} for ports 1 to 5 are shown in Fig. 5, along with the S_{11} of the transition for the sake of comparison. The ports are matched from 55.5 GHz to 71 GHz. The simulated

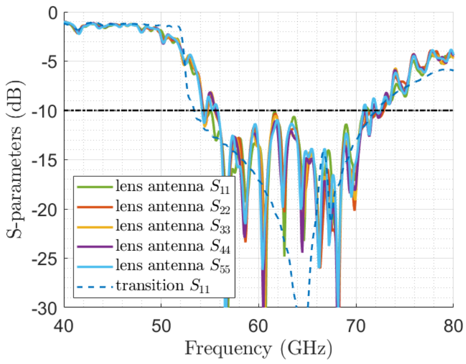

Fig. 5. Simulated S-parameters of the GRIN lens antenna.

radiation patterns at port 5 (not displayed here) show that a stable and symmetric fan-shaped beam is established from 56 GHz to 66 GHz, which represents a bandwidth 4 GHz wider than in our previous work [2], as shown at the bottom of Table I.

V. Mitigation of Whispering Gallery Modes

In [4] we proposed mitigation strategies to alleviate the undesired WGMs that arise in *Mismatched Luneburg Lenses* and make their performance more stable w.r.t. frequency. The two first strategies, i.e. using directive feeds and introducing absorbing elements (such as neighbouring feeds) are already implemented at this point as a *passive choice*: the transition presented in section III creates a directive source, and multiple feeds have been placed. We now implement the third strategy as an *active choice*: adding metallic elements inside the GRIN medium at carefully selected positions, that should at the same time block the paths that will end up as internal reflections, and leave unaltered the paths that will end up as the desired radiation.

The initial choice of positions can be guided by geometrical optics, which gives the analytical form of the ray paths inside *Mismatched Luneburg Lenses* in the form of conics [8] (in this particular case, ellipses). Fig. 4(b) shows the ray paths ending up as the desired radiation for port 7, while their repetition at ports 2-9 (not considering the dummy ports 1 and 10) produces the green zone, i.e. the zone which should not be perturbed. The rest of the lens is coloured as the red zone, travelled only by ray paths ending up as internal reflections. In that specific zone, we decided to place 6 metallic elements, represented as white circles, to damp the resonance of WGMs. In terms of fabrication, this means plating a few of the many through-holes drilled inside the lens dielectric body on PCB.

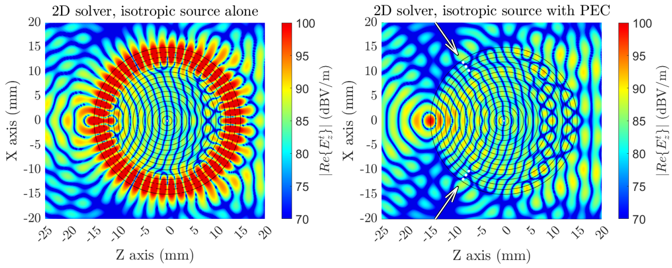

Fig. 6. Vertically polarized source, at 61.6 GHz, on the perimeter of a GRIN lens implementing $(\varepsilon_{center}, \varepsilon_{edge}) = (2.7, 2.2)$, with (right) and without (left) the introduction of the metallic elements (white circles).

Their effect can be further analysed with full-wave simulations, using the 2D solver presented in [4] allowing one to place PEC elements inside a GRIN lens. Fig. 6 compares simulations results at 61.6 GHz for an isotropic source placed on the perimeter of a lens implementing $(\varepsilon_{center}, \varepsilon_{edge}) = (2.7, 2.2)$, with and without the introduction of the metallic elements. At 61.6 GHz, the source alone results in a WGM with a strong resonance, which is efficiently damped with the introduction of the metallic elements, while the desired radiation is maintained as a flat wavefront.

VI. Measurements

Prototypes were fabricated and measured at the *WELCOME* facility at UCLouvain, with the same instruments as in [2]. Two GCPW to SIW transitions in a back-to-back configuration, as well as the GRIN lens antennas, were characterized. The comparison between measured and simulated S-parameters is summed up in Table II.

TABLE II
Comparison of the measurements with previous work.

	Previous work [2]	This work
Sim. transition insertion loss	2 dB	1.2 dB
Meas. transition insertion loss	2.5 dB	1.7 dB
Frequency shift	1 GHz	0.1 GHz
Sim. lens impedance matching	$>$ 58.5 GHz	$>$ 55.5 GHz
Meas. lens impedance matching	$>$ 61 GHz	$>$ 56 GHz
Frequency shift	3.5 GHz	0.5 GHz

For the GCPW to SIW transitions, practically no frequency shift ($\leq$ 0.1 GHz) can be observed in terms of S_{21} between measurements and simulations, while a few additional losses arise, especially around 64 GHz. We estimate that the transition itself accounts for 0.5 dB of additional losses. The impedance matching is even lower in measurements than what was simulated. Compared to our previous work [2], the measured insertion losses of the transition are 0.8 dB lower, and the frequency shift is reduced by a factor 10 (see Table II).

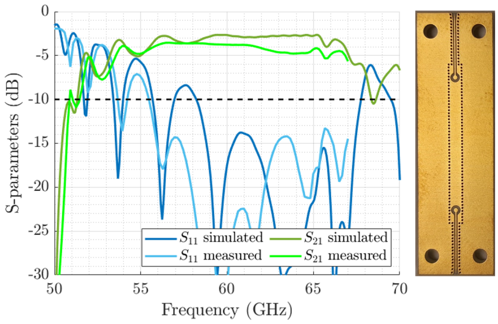

Fig. 7. Simulated and measured S-parameters (left) of the two GCPW to SIW transitions in a back-to-back configuration (right).

Prototypes of the GRIN lens antenna were also printed and one of them is shown in Fig. 8. It was measured (see Fig. 9, Fig. 10 and 11), both without (dark blue curves) and with the metallic elements (orange curves). Those measurements will be compared with CST simulations of the version without the metallic elements (light blue curves).

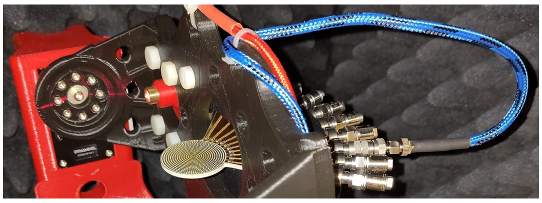

Fig. 8. Fabricated GRIN lens antenna in the ®MilliBox anechoic chamber.

The comparison between measured and simulated S-parameters is given in Fig. 9 for ports 1, 3 and 5. We observe

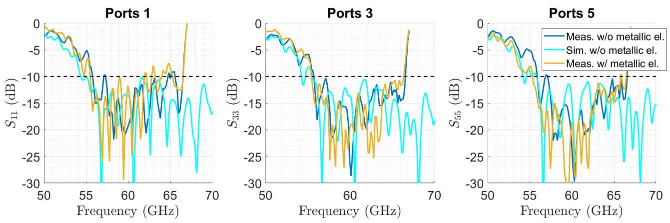

Fig. 9. Simulated and measured S-parameters at ports 1, 3 and 5.

very good agreement with a matching above 56 GHz, i.e. with a frequency shift $\leq$ 0.5 GHz w.r.t. simulations, much reduced compared to our previous work [2] (see Table II). That shift is slightly further reduced with the addition of the metallic elements, that do not perturb the matching bandwidth (except for port 1, as expected from Fig. 4). The sharp increase at 67 GHz can be explained by the time gating that had to be applied on the measured data.

Radiation patterns were measured up to 70 GHz and, as in our previous work [2], time gating and Gaussian filtering were applied over the data. The radiation patterns obtained at port 5 are shown in Fig. 10 at multiple frequencies. We

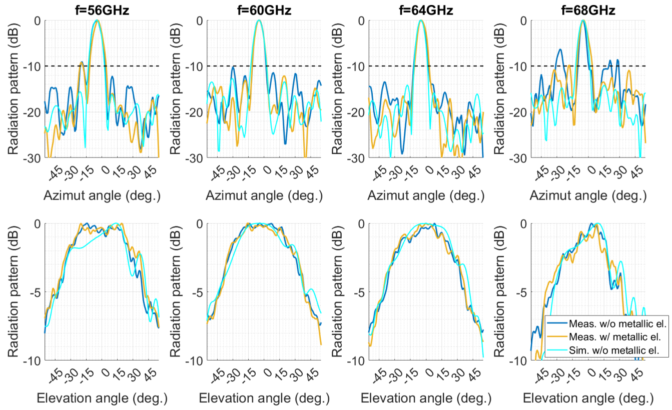

Fig. 10. Simulated and measured radiation patterns for port 5 (H-plane cuts above, E-plane cuts below) at multiple frequencies.

observe good agreement with simulations in both planes. In the H-plane, the beamwidth is equal to the simulated value, and the sidelobe level (SLL) is slightly higher even though its remains below -10 dB within the bandwidth of interest. The introduction of the metallic elements decreases the SLL on the average, while the beamwidth is unaltered. In the E-plane, there is good agreement with the simulated patterns: the larger beamwidth is observed at 56 GHz, 60 GHz and 64 GHz, with much better symmetry than in our previous work [2]. The introduction of the metallic elements has little effect in this plane, yet they slightly enlarge the beamwidth at some frequencies, such as 56 GHz, which typically comes with a SLL reduction.

Radiation patterns were also measured for all ports. The H-plane cuts are shown for ports 1, 3 and 5 in Fig. 11 at 62 GHz, confirming the collimation effect. We observe a very good

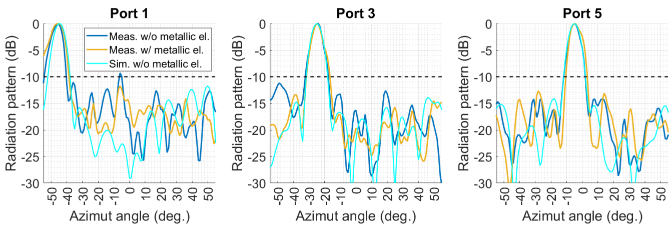

Fig. 11. Simulated and measured radiation patterns for ports 1, 3 and 5 (H-plane cuts) at 62 GHz.

agreement with simulations for the collimated beamwidth, as well as SLL below -10 dB for ports 3 and 5. The introduction of the metallic elements decreases the power radiated outside of the main beam on the average, while the beamwidth is unaltered. This confirms their relevant positions which allow them not to perturb the collimation from any of the ports.

Eventually, the evolution of key performance indicators over frequency was calculated for port 5 and is shown in Fig. 12. In the H-plane (az), the measured beamwidth is stable and very close to simulated values, as well as unaltered by the metallic elements. The side lobes remain below -10 dB between 56 GHz and 67 GHz, except for a small upward peak close to 60 GHz. The latter is damped thanks to the introduction of the metallic elements, which cause the SLL to decrease for all frequencies from 56 GHz to 66 GHz.

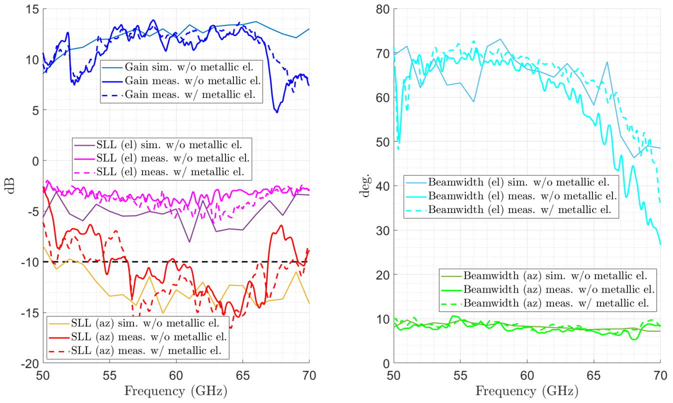

Fig. 12. Simulated and measured key performance indicators at port 5.

In the E-plane (el), the measured beamwidth is large and follows the simulated trend, although with a value going below 60° after 64 GHz. The introduction of the metallic elements enlarges that beamwidth on the average, hence the bandwidth where the beamwidth stays above 60° increases up to 66 GHz. The side lobes in that plane are slightly higher than in simulations, and the introduction of the metallic elements helps decreasing them a little (especially from 60 GHz to 65 GHz), which typically comes with beamwidth enlargement.

Eventually, the measured (relative) gain is normalized to a maximum of 14 dB for the sake of comparison with the simulated (absolute) gain. The trend shows good agreement with an increase up to 56 GHz (even though with a discontinuity at 52 GHz that does not appear in simulations) followed by a plateau between 56 GHz and 66 GHz, after which the gain decreases (faster than in simulations). The introduction of the metallic elements damps the gain variations inside the plateau, i.e. it stabilizes the performance over frequency.

TABLE III
COMPARISON OF THE KPI ON THE BANDWIDTH [56 GHZ, 66 GHZ].

	Without metallic el.	With metallic el.
Gain (± std)	± 0.70 dB	± 0.50 dB
SLL el (mean ± std)	-3.65 dB ± 0.43 dB	-4.68 dB ± 0.62 dB
SLL az (mean ± std)	-12.22 dB ± 1.60 dB	-13.60 dB ± 1.62 dB
BW el (mean ± std)	63.21° ± 5.29°	67.17° ± 2.56°
BW az (mean ± std)	7.66° ± 0.67°	8.28° ± 0.65°
Stable fan shape	[56 GHz, 64 GHz]	[56 GHz, 66 GHz]

To sum up, the fan-shaped beam is formed on the 8 GHz frequency band [56 GHz, 64 GHz] with a plateau of gain, side lobes below -10 dB in the H-plane and a beamwidth above 60° in the E-plane. That frequency band is enlarged to [56 GHz, 66 GHz], i.e. by 2 GHz, thanks to the introduction of the metallic elements. To illustrate this, the measured key performance indicators, averaged over [56 GHz, 66 GHz], are compared in Table III. The introduction of the metallic elements stabilizes the plateau of gain by reducing its standard deviation, decreases the SLL and (slightly) enlarges the beamwidth in both planes.

VII. CONCLUSION

The theoretical and numerical work [4] conducted on *Mismatched Luneburg Lenses* with a 2D full-wave cylindrical solver, predicted a stabilization of the gain performance w.r.t. frequency thanks to carefully positioned metallic elements inside the lens, as well as a slight increase of the collimated beamwidth (H-plane). This has been demonstrated here with the measurements of a 3D practical realization of a GRIN lens antenna on PCB, with metallic elements embodied as plated through-holes. This work provides additional insightful information about the effect of such metallic elements in the other plane (E-plane) that could not be predicted in 2D, such as a SLL decrease and a beamwidth enlargement in the E-plane. Compared to our previous work [2], the new choice of substrate led to a 3 GHz increase in the bandwidth where the fan-shaped beam is stable, while the introduction of the metallic elements led to an additional 2 GHz increase, eventually resulting in a GRIN lens antenna matched in impedance and with a stable radiation pattern over a 10 GHz band.

ACKNOWLEDGMENT

This work was conducted thanks to the collaboration between the ICTEAM Research Group and BEA Sensors Europe, and was funded by the Région Wallonne under the "Doctorat en entreprise" framework of the SPW EER.

REFERENCES

[1] R. K. Luneburg, *Mathematical Theory of Optics*, Berkeley, CA, USA: Univ. California Press, 1964.

[2] V. Kaschten, D. Lederer, and C. Craeye, "A cylindrical mismatched Luneburg lens implemented on PCB at V-band," 18th European Conference on Antennas and Propagation (EuCAP), Glasgow, UK, 2024.

[3] O. Zetterstrom, N. J. G. Fonseca, and O. Quevedo-Teruel, "Collimating truncated virtual image lens," IEEE Trans. Antennas Propag., vol. 72, no. 5, pp. 3928-3937, May 2024.

[4] V. Kaschten, D. Tihon, D. Lederer, and C. Craeye, "Mismatched Luneburg lenses: numerical analysis and design rules," IEEE Trans. Antennas Propag., vol. 72, no. 5, pp. 4487-4500, May 2024.

[5] S. Clendinning et al., "Reducing the refractive index range of GRIN lenses through the integration of a reflectarray," 17th European Conference on Antennas and Propagation (EuCAP), Florence, Italy, 2023.

[6] A. V. Boriskin, and A. I. Nosich, "Whispering-gallery and Luneburg-lens effects in a beam-fed circularly layered dielectric cylinder," *IEEE Trans. Antennas Propag.*, vol. 50, no. 9, pp. 1245-1249, Sep. 2002.

[7] B. C. Chen, Y. M. Pan, and S. Y. Zheng, "Truncated 2-D Gutman lens antenna with planar feeding surface for stable wide-angle beam scanning in millimeter-waveband," IEEE Trans. Antennas Propag., vol. 71, no. 11, pp. 9030-9035, Nov. 2023.

[8] V. Kaschten, D. Lederer, and C. Craeye, "Ray paths and frequency dependence of mismatched Luneburg lenses", submitted to IEEE Trans. Antennas Propag.

[9] F. Maggiorelli et al., "Profile inversion and closed form formulation of compact GRIN lenses," IEEE Open Journal of Antennas and Propagation, vol. 2, pp. 315-325, Feb. 2021.

[10] Q. Liang et al., "Design of compact Rotman lens using truncated ports with energy distribution slots," IEEE Access, vol. 7, pp. 120766-120773, June 2019.